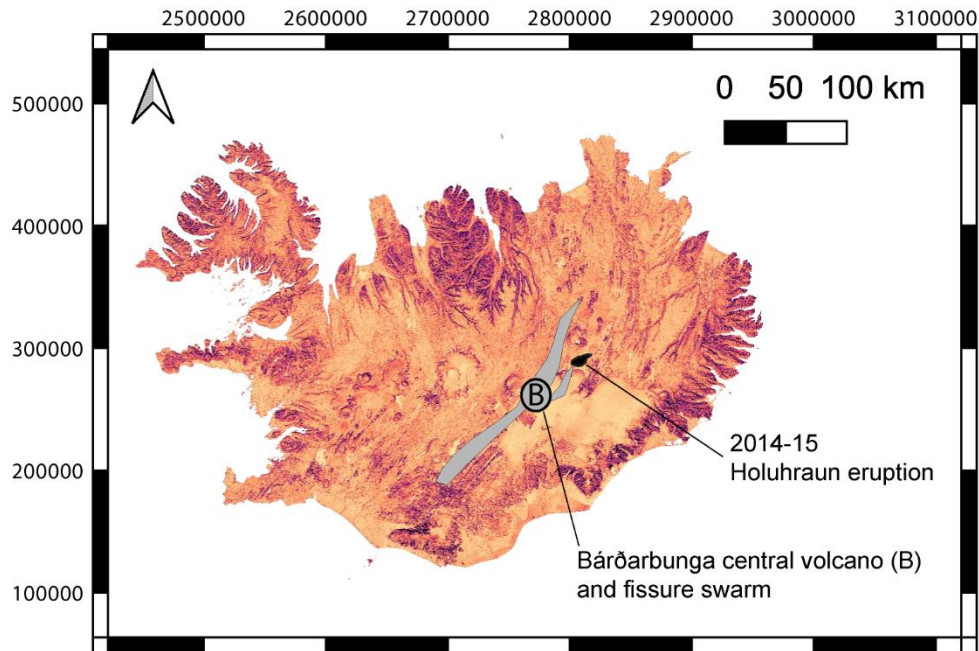# Supplementary Material

## 1. Figures



**Supplementary Figure S1:** Location map showing the 2014-15 Holuhraun eruption site, Iceland. Black shaded region indicates the extent of the extrusive lava flows. Grey shaded region shows Bárðarbunga central volcano (B) and fissure swarm (modified from Halldorsson et al., 2018). Map figure produced in QGIS using the EPSG: 8088 (ISN2016) coordinate reference system. Data from the National Land Survey of Iceland (https://atlas.lmi.is).
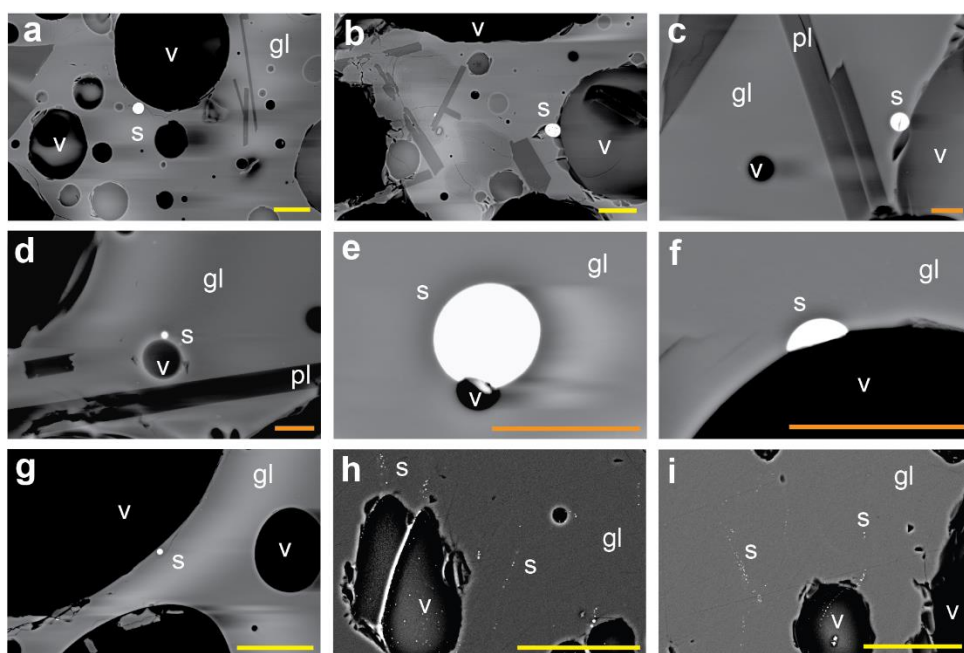
**Supplementary Figure S2:** Additional backscattered-electron SEM images showing the relationships between sulfides and vesicles/bubbles. Annotations are abbreviated to sulfides (s), vesicles (v), silicate glass (gl), plagioclase (pl); (h, i) Trails of small sulfide globules are sometimes observed in association with vesicles. Scale bars indicate 50 µm (yellow) or 10 µm (orange). Images taken from all samples.
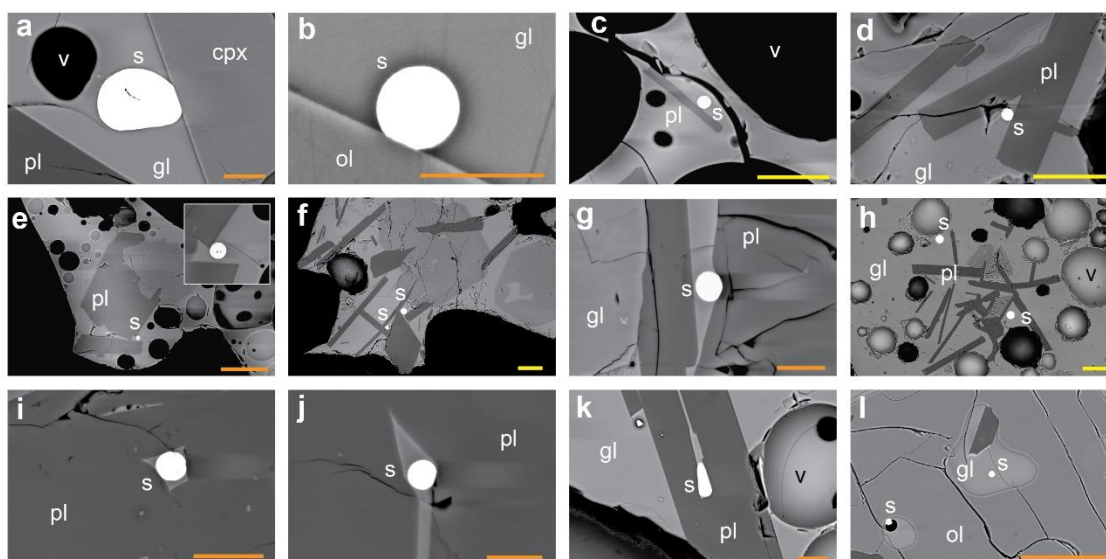
**Supplementary Figure S3:** Additional backscattered-electron SEM images showing the relationships between sulfides and crystals. Annotations are abbreviated to sulfides (s), vesicles (v), silicate glass (gl), plagioclase (pl), olivine (ol), clinopyroxene (cpx). Scale bars indicate 50 µm (yellow) or 10 µm (orange). Images taken from all samples.
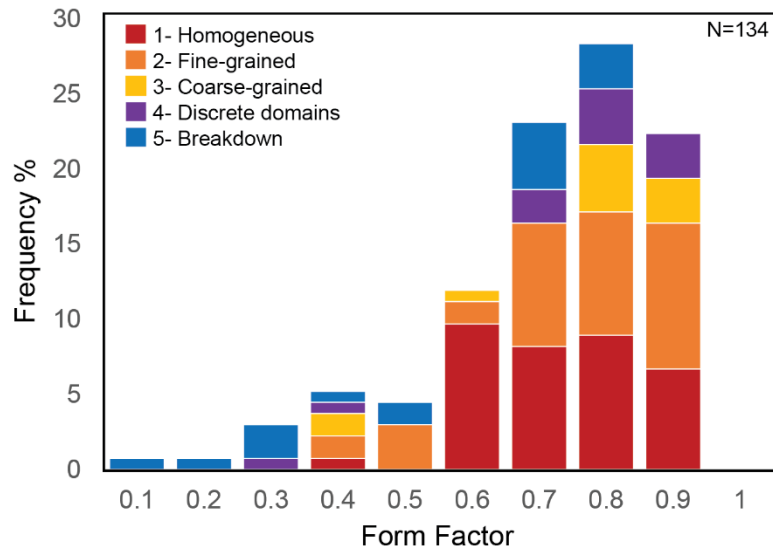
**Supplementary Figure S4:** Shape distribution of sulfide globules. Shape is described by Form Factor (see main text for definition). Irregularity decreases from left to right, with a value of 1 representing a perfect circle. The colour scheme sub-divides the sulfide population according to their textural classification, and is the same as for Figure 4. Data include all three samples.
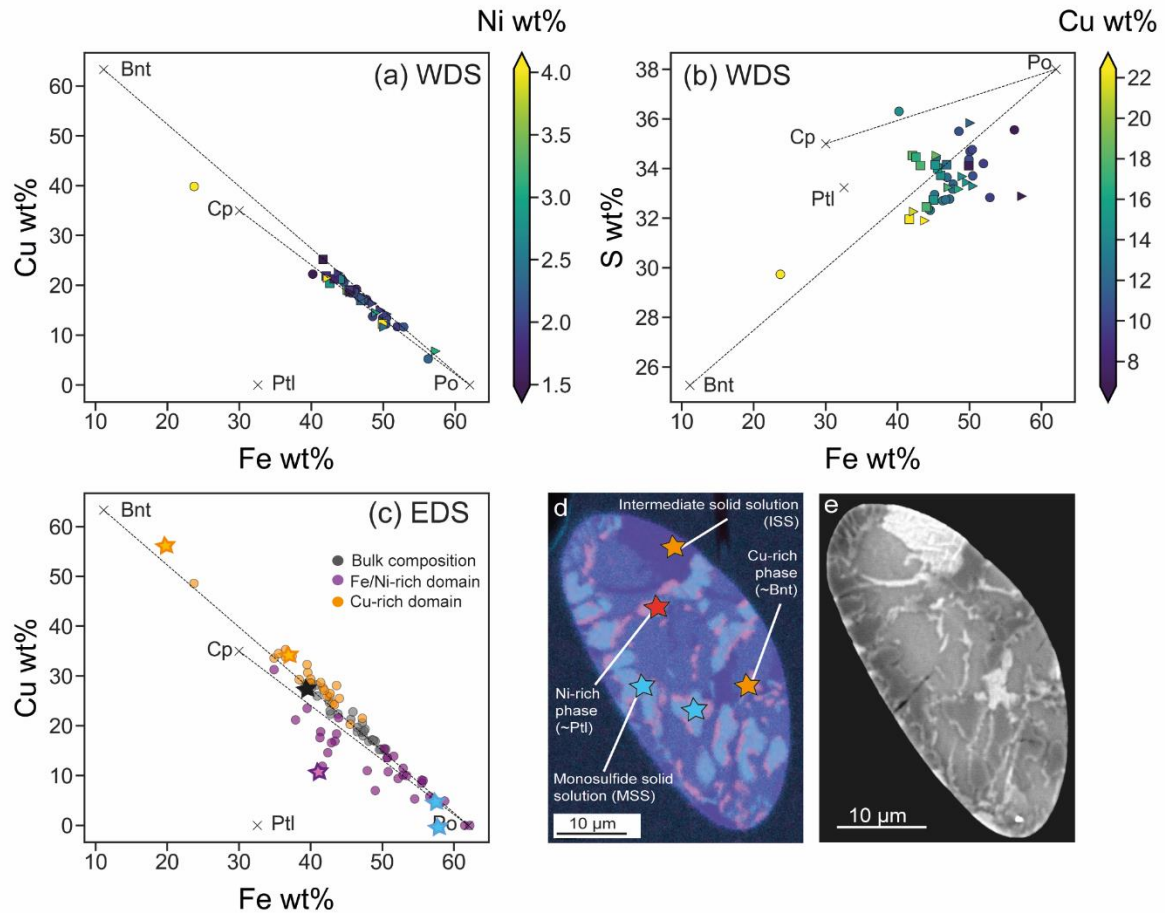
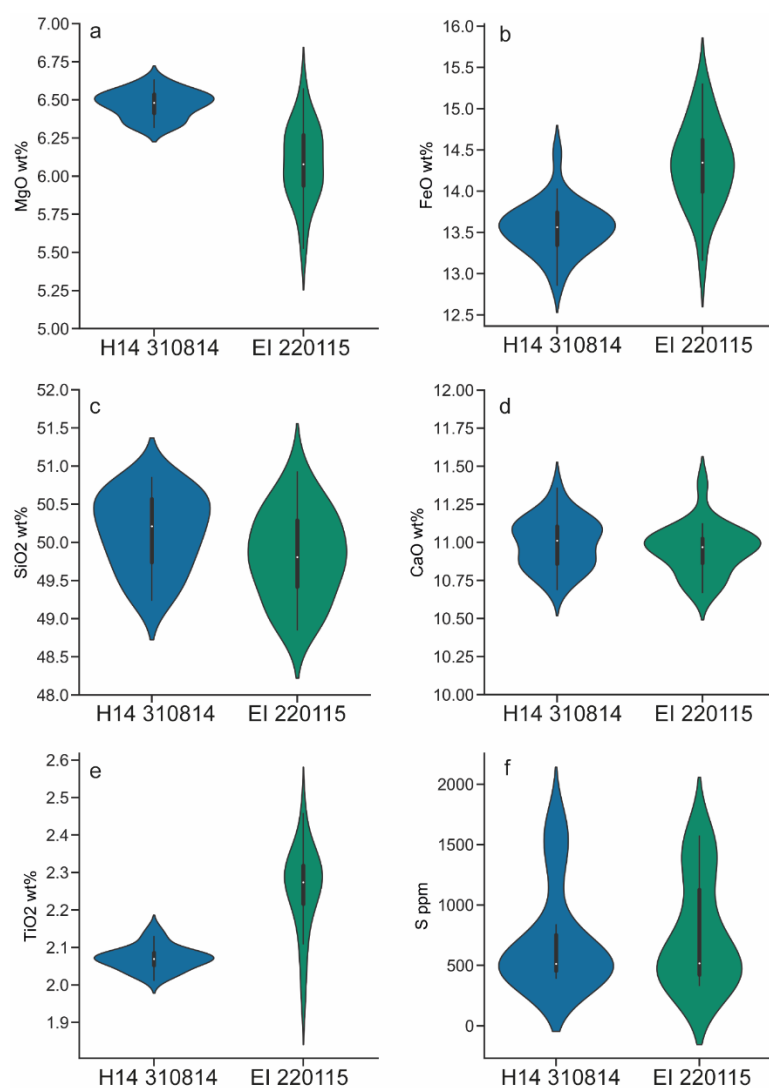**Supplementary Figure S5:** (a, b) Bulk compositions of the sulfide liquid for H14 (31 August 2014; circles), MSR (29 October 2014; squares) and EI (22 January 2015; triangles). Bulk sulfide compositions are reconstructed from electron microprobe WDS analyses; see main text for methods. (c–e) Compositions of discrete domains with individual sulfide globules, as measured by EDS. Circles show data from all analyses. Stars represent analyses from the single sulfide globule shown in the EDS map (d) and backscattered electron SEM image (e). Stoichiometric compositions of sulfide mineral phases are shown for reference, including pyrrhotite (Po), chalcopyrite (Cp), bornite (Bnt), and pentlandite (Ptl).
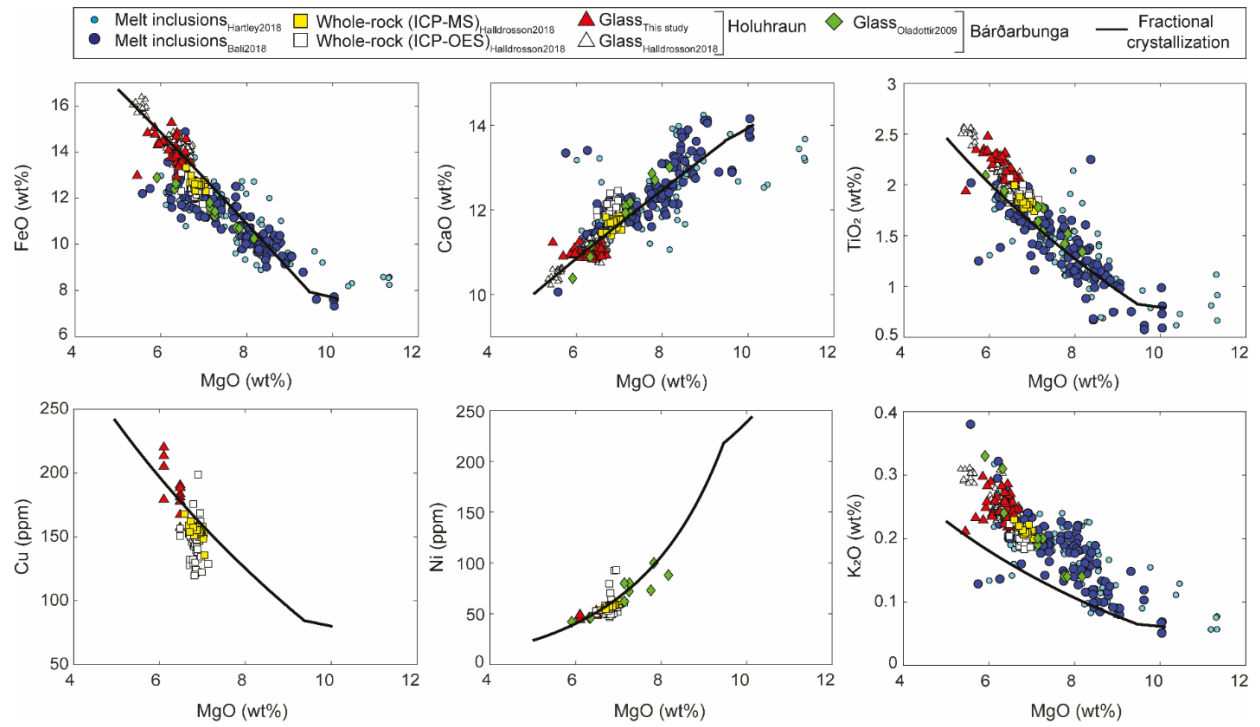
**Supplementary Figure S6:** Whole rock, melt inclusion and matrix glass compositions from Holuhraun and Barðarbunga (this study; Oladottir, 2009; Hartley et al., 2018; Bali et al., 2018; Halldorsson et al., 2018) are well matched for most elements by the Petrolog3 models (see main text for details).

**Supplementary Figure S7:** Matrix glass compositions in August 2014 (H14; n=26) and January 2015 (EI; n=20). Violin plots display the statistical features of a box plot (white dot = median; thick black bar = interquartile range; thin black bar = low/upper adjacent values), whilst also visualising the entire distribution as a kernel density plot (shaded region).
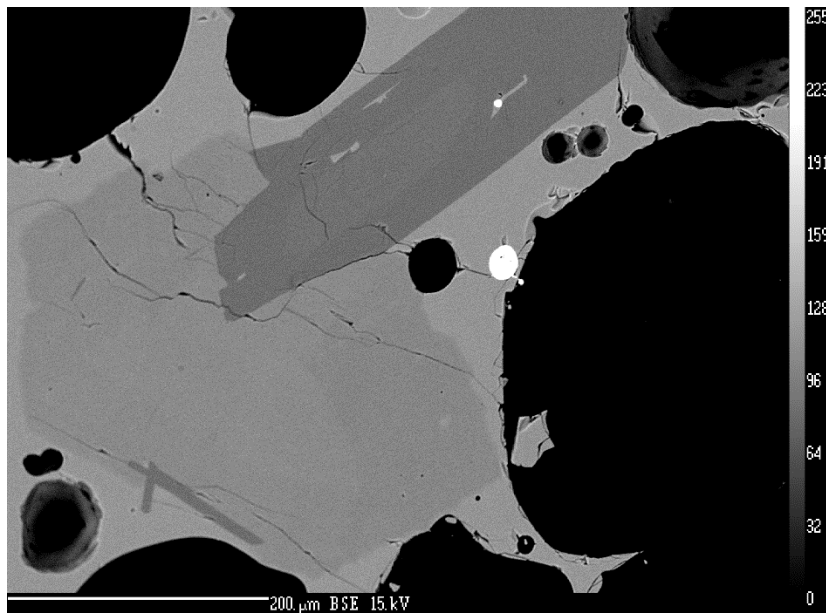
**Supplementary Figure S8:** Zoned plagioclase phenocryst with An-rich core composition (An = 83) and a sulfide inside a melt inclusion within the outer, lower-An rim (An = 0.70). The size of the sulfide is larger than could be produced by post-entrapment modification of the melt inclusion, and therefore indicates entrapment of a sulfide globule already present in the melt.
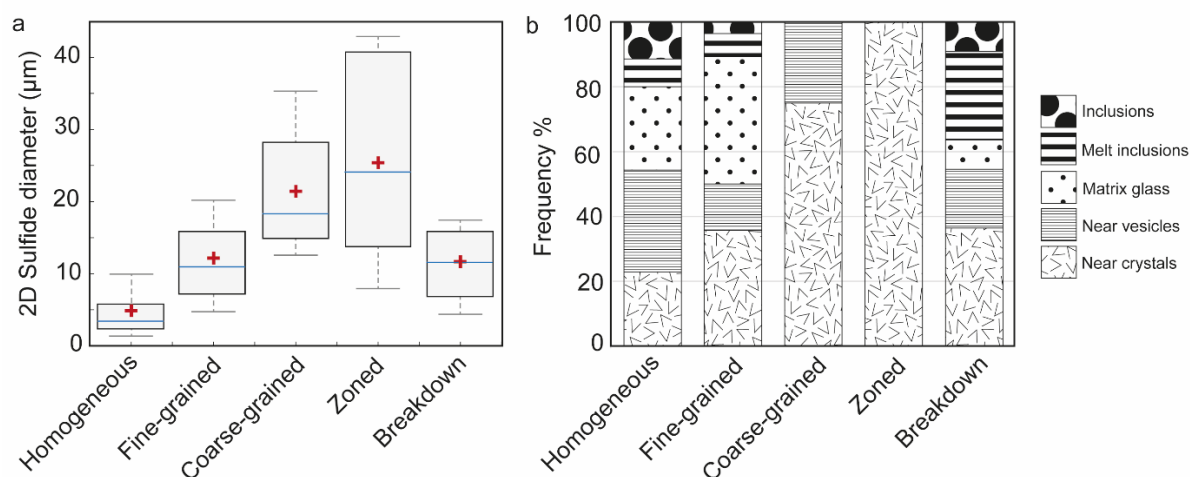
**Supplementary Figure S9: (a)** The relationship between sulfide texture and globule size. The boxes represent the interquartile range, whilst whiskers extend to show the complete range of the distribution. Red crosses and blue horizontal lines show the mean and median values of the distribution, respectively; n= 46 (homogenous), 43 (Fine-grained), 13 (Coarse-grained), 14 (Zoned), and 18 (Breakdown). Note that size is expressed as the 2D diameter of an area-equivalent circle, as measured by image analysis, without stereological correction. Textural classification is as illustrated in Figure 5. Data are based on all three samples. **(b)** The relationship between sulfide texture and spatial location. The proportion of sulfides within each spatial group are expressed as a percentage of the total number of sulfides in each textural class; n= 35 (Homogenous), 28 (Fine-grained), 4 (Coarse-grained), 6 (Zoned), and 11 (Breakdown). Data are from all three samples.
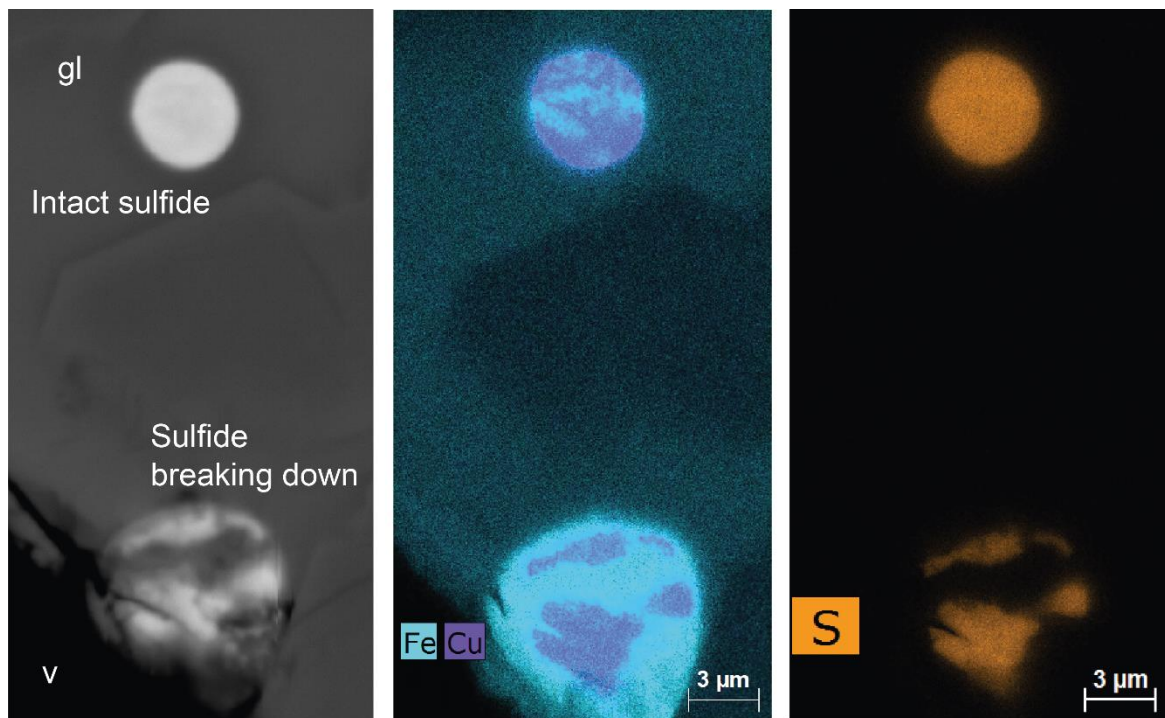
**Supplementary Figure S10:** Comparison of intact sulfide globule versus one breaking down. Note that that the sulfide breaking down is next to a vesicle wall. The resorbing sulfide is Fe-rich, relative to the Cu- and S-rich intact globule.
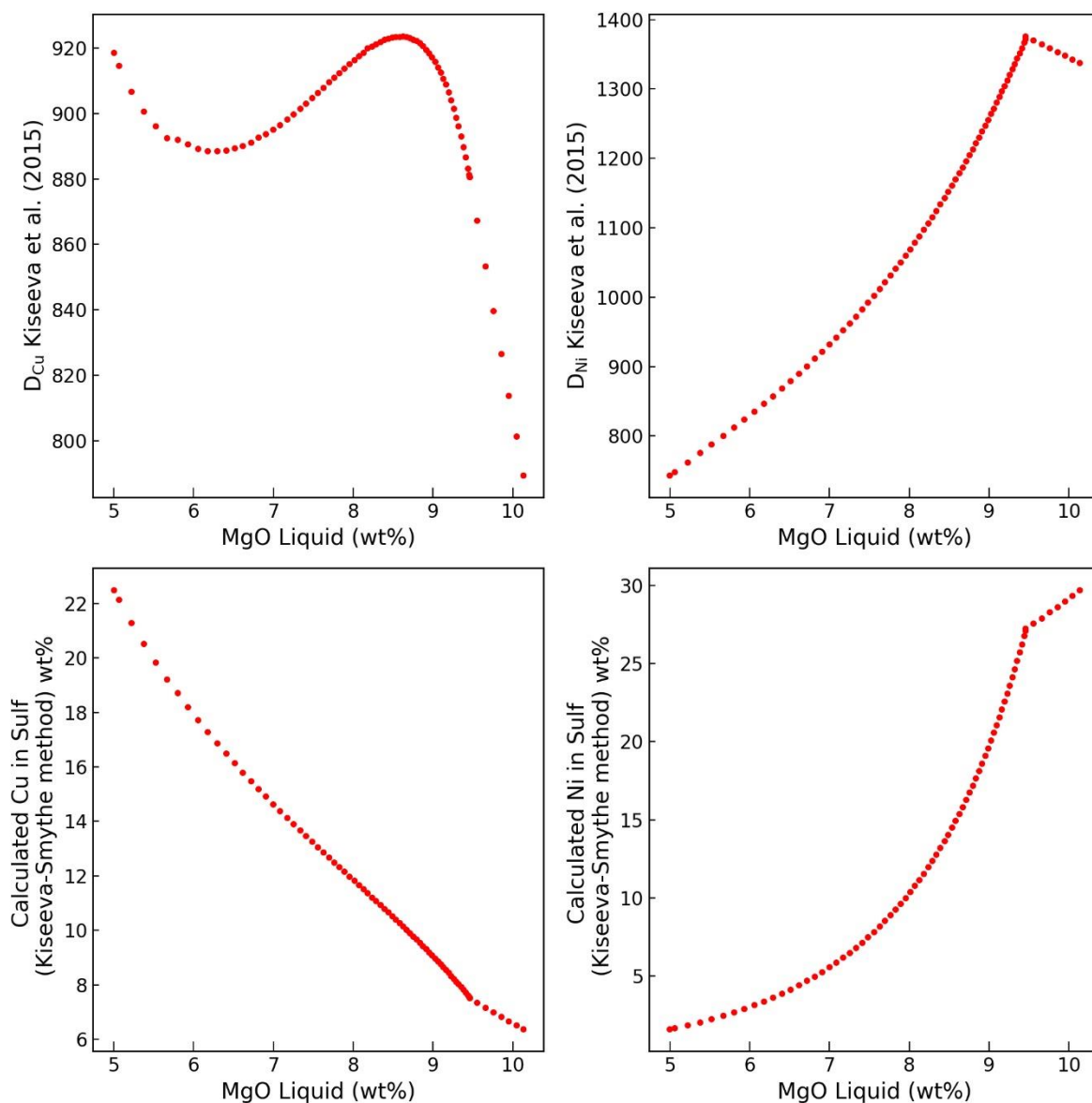
**Supplementary Figure S11:** Modelled evolution in sulfide bulk composition as a function of melt crystallisation. (a, b) Variation in the sulfide-silicate melt partition coefficient (D) for Cu and Ni, respectively, as a function of melt MgO content, based on Kiseeva et al., (2015). (c, d) Calculated Cu and Ni content of the equilibrium sulfide liquid as a function of melt MgO content. Sulfide bulk compositions are predicted to become increasingly Cu-rich and Ni-poor as crystallisation progresses.
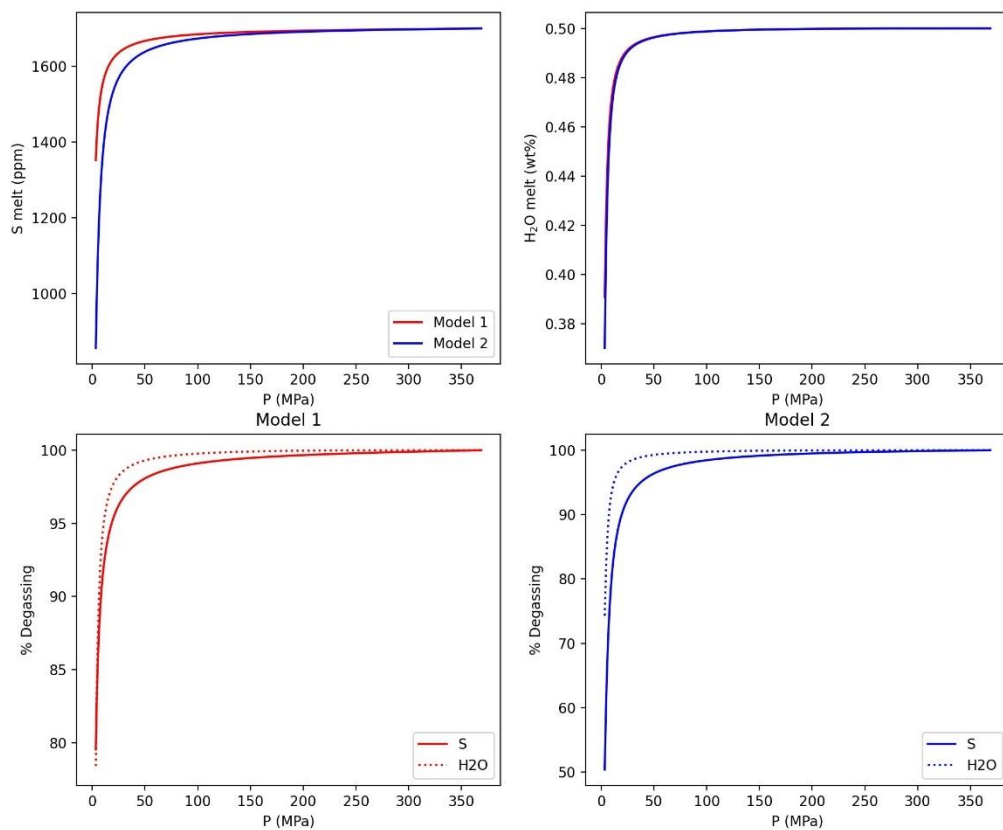
**Supplementary Figure S12:** Modelled dissolved volatile contents ($CO_2$-S) from Sulfur_X (Ding et al. 2022). Model 1 and model 2 parameters described in Supplementary Note 4. Model results are truncated at 3 MPa, because of instability in the S partition coefficient at lower pressures.

**2. Data Tables**

**Attached spreadsheet**

**Table S1:** Details of the selected samples used in this study. All samples are rapidly quenched tephra collected close to the eruptive vent soon after eruption. Sample IDs correspond to those defined in Bali et al (2018) and Hartley et al (2018), as these represent splits of the same samples.

**Table S2: Glass analyses by electron microprobe.** All analyses shown as weight percent oxides.

**Table S3: Precision and accuracy.** Precision and accuracy for EPMA analyses of matrix glasses and mineral phases, calculated from repeat measurements of VG2 (basaltic glass), A99 (basaltic glass), Labradorite, Augite, and San Carlos Olivine (SCO) secondary standards.

**Table S4: Glass analyses LA-ICPMS.** All analyses shown in ppm unless otherwise stated.

**Table S5: Mineral compositions by electron microprobe** (plagioclase, clinopyroxene, and olivine). All analyses shown as weight percent oxides.

**Table S6: Sulfide compositions by WDS (electron microprobe)**. All analyses shown as weight percent oxides.

**Table S7: Calculated sulfide bulk compositions from electron microprobe analyses.** All analyses shown as weight percent oxides.

**Table S8: Sulfide compositions by EDS (SEM)**. All analyses shown as weight percent oxides.

**Table S9: Line profiles in glass away from sulfides.** Spot size 10 microns. Spot spacing 12.5 microns. All analyses shown as weight percent oxides.

**Table S10: Sulfide size distribution and stereological correction.** Data used in Figure 3.

**Table S11: Sulfide textures and spatial distribution.** Data used in Figures 1, 4 and 6.

**Table S12-13: Sulfur_X degassing models.**

## 3. Supplementary methods

**Supplementary Note 1: Analytical conditions for electron microprobe microanalysis (EPMA)**

Major, minor and volatile (S and Cl) element concentrations in matrix glass, sulfides, and silicate mineral phases were measured on carbon-coated polished grain mounts using a Cameca SX100 electron microprobe (EPMA) at the University of Cambridge, UK. Glass analyses were performed under dual-conditions: Condition 1 (major elements): 15 kV, 10 nA, 10 µm defocused beam; Condition 2: 15 kV, 40 nA, 10 µm. Olivine: 15 kV, 20 nA, and 1 µm beam size. Clinopyroxene: 15 kV, 20 nA, and 1 µm beam size. Plagioclase: 15 kV, 10 nA, and 5 µm beam size. Sulfide analyses were performed under operating conditions of 20 kV, 40 nA, and either a 10 µm or 1 µm beam size. Full conditions and counting times are reported in **Table S13** (**supplementary materials**).

We used a combination of mineral and glass standards for primary calibration. Repeat analyses of Smithsonian basaltic glass reference materials (VG2, Juan de Fuca Ridge, NMNH 111240-52; VGA-99, Mahaopuhi lava lake, Hawaii, NMNH 113498-1; San Carlos Olivine; Augite; Labradorite; Anorthite) were used to monitor instrumental drift, for which no post-processing corrections were required. Precision on glass analyses is <3% for Si, Mg, Na, Al, Fe, Ca, Ti, S; <10% for K and P, and <20% for Mn. Accuracy relative to in-house basaltic glass standards (VG2, VGA99) is $< \pm 1\%$ for all elements except Na, $S < \pm 5\%$; $Mn < \pm 10\%$; $P < \pm 15\%$ (**Table S3, supplementary materials**). Precision is reported as one standard deviation of all repeats divided by the mean and accuracy as the mean of all repeats divided by the standard reference composition.

**Table S13: Electron microprobe operating conditions for major elements and minerals**

| Element | Condition | Crystal | Time on peak (s) | Time on background (s) | Calibration standard |
|---------|-----------|---------|------------------|------------------------|----------------------|
| *Glass* | | | | | |

| | | | | | |
|---|---|---|---|---|---|
| Si | 1 | TAP | 10 | 5 | Diopside |
| Mg | 1 | TAP | 30 | 15 | St Johns Olivine |
| Na | 1 | LTAP | 10 | 5 | Jadeite |
| Al | 1 | LTAP | 30 | 15 | Corundum |
| K | 1 | LPET | 10 | 5 | K-Feldspar |
| Fe | 1 | LIF | 20 | 10 | Fayalite |
| Cr | 1 | LIF | 40 | 20 | Cr |
| Mn | 1 | LIF | 40 | 20 | Mn |
| Ca | 1 | PET | 20 | 10 | Diopside |
| Ti | 1 | LPET | 40 | 20 | Rutile |
| P | 1 | PET | 30 | 15 | Apatite |
| S | 2 | LPET | 120 | 60 | Pyrite |
| Olivine | | | | | |
| Si | | TAP | 10 | 5 | Diopside |
| Mg | | TAP | 20 | 10 | St Johns Olivine |
| Al | | LTAP | 120 | 60 | Corundum |
| P | | PET | 60 | 30 | Apatite |
| Ca | | LPET | 120 | 60 | Diopside |
| Ti | | PET | 60 | 30 | Rutile |
| Fe | | LIF | 20 | 10 | Fayalite |
| Ni | | LIF | 60 | 30 | NiO |
| Cr | | LIF | 40 | 20 | Cr |
| Mn | | LIF | 40 | 20 | Mn |
| Plagioclase | | | | | |
| Si | | TAP | 10 | 5 | Diopside |
| Na | | LTAP | 10 | 5 | Jadeite |
| K | | LPET | 10 | 5 | K-feldspar |
| Fe | | LIF | 40 | 20 | Fayalite |
| Cr | | LIF | 40 | 20 | Cr |
| Mn | | LIF | 40 | 20 | Mn |
| Ca | | PET | 20 | 10 | Diopside |
| Ti | | LPET | 60 | 30 | Rutile |
| Mg | | LTAP | 60 | 30 | St Johns Olivine |
| Al | | TAP | 10 | 5 | Corundum |
| Clinopyroxene | | | | | |
| Si | | TAP | 10 | 5 | Diopside |
| Mg | | TAP | 20 | 10 | St Johns Olivine |
| Na | | LTAP | 10 | 5 | Jadeite |
| Al | | LTAP | 60 | 30 | Corundum |
| K | | LPET | 10 | 5 | K-Feldspar |
| Fe | | LIF | 20 | 10 | Fayalite |
| Cr | | LIF | 60 | 30 | Cr |
| Mn | | LIF | 40 | 20 | Mn |
| Ca | | PET | 20 | 10 | Diopside |
| Ti | | LPET | 60 | 30 | Rutile |
| Sulfides | | | | | |
| S | | PET | 20 | 10 | Pyrite |
| Fe | | LIF | 20 | 10 | Fayalite |
| Ni | | LIF | 60 | 30 | NiO |
| Cu | | LIF | 60 | 30 | Cu |

**Supplementary Note 2: Analytical metadata for laser ablation inductively coupled plasma mass spectrometry (LA-ICP-MS)**. Adapted from http://www.plasmage.org/recommendations.

| Laboratory & Sample Preparation | |
|---|---|
| Laboratory name | School of Environment, Earth and Ecosystem Sciences, Open University, UK |
| Sample type/mineral | Matrix glass |
| Sample preparation | Tephra (silicate particles) mounted in epoxy |
| **Laser ablation system** | |
| Make, Model & type | Photon Machines Analyte G2 193 nm excimer laser |
| Ablation cell & volume | HelEx II 2-volume cell |
| Laser wavelength (nm) | 193 nm |
| Pulse width (ns) | 4 ns |
| Fluence (J/cm$^2$) | 3.63 J/cm$^2$ |
| Repetition rate (Hz) | 10 Hz |
| Ablation duration (s) | 30 s |
| Spot diameter (μm) | 50 & 65 μm |
| Sampling mode / pattern | static spots |
| Carrier gas | 100% He in the cell; 5 ml/min $N_2$ added via a y-connector prior Ar make-up gas combined in a mixing bulb down stream |
| Cell carrier gas flow (l/min) | 0.9 l/min He |
| **ICP-MS Instrument** | |
| Make, Model & type | Agilent 8800 ICP-QQQ-MS |
| Sample introduction | Ablation aerosol in He & Ar gas mix |
| RF power (W) | 1250 W |
| Ar carrier gas flow (l/min) | 0.83 l/min (optimised for sensitivity) |
| Detection system | Dual-mode discrete dynode electron multiplier |
| Masses measured; Integration time per peak/dwell times (ms) | $^{29}$Si 0.005; $^{43}$Ca 0.005; $^{51}$V 0.008; $^{59}$Co 0.008; $^{60}$Ni 0.008; $^{65}$Cu 0.008; $^{66}$Zn 0.008; $^{88}$Sr 0.008; $^{90}$Zr 0.008; $^{93}$Nb 0.008; $^{95}$Mo 0.01; $^{111}$Cd 0.03; $^{115}$In 0.03; $^{118}$Sn 0.03; $^{121}$Sb 0.03; $^{133}$Cs 0.03; $^{137}$Ba 0.008; $^{139}$La 0.008; $^{147}$Sm 0.08; $^{153}$Eu 0.008; $^{157}$Gd 0.008; $^{172}$Yb 0.008; $^{175}$Lu 0.008; $^{182}$W 0.03; $^{205}$Tl 0.03; $^{208}$Pb 0.03; $^{209}$Bi 0.03 |
| Total integration time (s) | 0.5509 |
| Gas blank | 30 seconds |
| Washout | 50 seconds |
| **Data Processing** | |
| Calibration strategy | SRM-NIST 612 every ~15 analyses. |
| Reference Material info | SRM-NIST 612 (Jenner and O'Neill, 2012) BCR-2G (Jenner and O'Neill, 2012) |
| Data processing package used | Iolite v3.71; DRS: X_Trace_Elements_IS; internal standard $^{29}$Si |
| Uncertainty level & Quality control / Validation | BCR-2G within 10% of the preferred value depending on element concentration, ablation diameter and homogeneity of different BCR-2G chips. |

**Supplementary Note 3: Sulfide texture as an indicator of undercooling and crystallisation timescales**

Sulfide texture is a size-dependent process controlled by a balance between the amount of undercooling and the time between MSS and ISS crystallisation (Patten et al., 2012). The nucleation rate of sulfide crystals within sulfide liquid droplets depends on the degree of undercooling, where high degrees of undercooling promote delayed but rapid crystallisation. Fine-grained sulfides contain numerous nucleation sites within the droplet but the characteristic intergrowth of MSS and ISS indicate insufficient time was available to grow large crystals by diffusion. Coarse-grained sulfides are texturally similar but have fewer nucleation sites and more rapid crystallisation. In contrast, zoned sulfides have well-developed compositional segregation, with the largest grains containing fully developed crystals of bornite and pyrrhotite (**Figs. 6 and 8, main text**). This zoned texture requires sufficient time between the first crystallisation of MSS and solidification of the droplet for the fractionated Cu-Fe-rich liquid to migrate away and crystallise ISS, implying relatively low degrees of undercooling. The effective solubility of MSS is greatest in smaller sulfide droplets, and therefore these droplets require higher degrees of undercooling for crystallisation to occur (Patten et al., 2012); this is borne out in our data, as sulfide textures exhibit a marked size-dependence (**Fig. 7, main text**). The surface roughness of sulfide globules (i.e. whether smooth or crenulated) may help to indicate whether the droplet remained molten, or had begun to crystallise, at the moment the melt quenched past the glass transition (Czamanske and Moore, 1977). However, crystallised sulfides may also exhibit smooth outlines (e.g., Rottier et al., 2020, 2019). In the Holuhraun pyroclasts, homogenous and fine-grained sulfides represent 75% of the total sulfide population in the early erupted sample. High effusion rates and lava fountaining early in the eruption may have promoted rapid and abundant sulfide nucleation and high degrees of undercooling, limiting the opportunity for compositional segregation. Zoned sulfides comprised only ~5% of the sulfide population in the early erupted sample but ~20% of the population in later samples from November and January (**Fig. 5, main text**). We suggest that the lower magma effusion rates as the eruption progressed may have provided additional time for compositional segregation within the sulfide liquid prior to eruption and quenching.

**Supplementary Note 4: Modelling Degassing**

We use the S-C-H degassing model Sulfur_X (Ding et al. 2023) to track the relative onset of $H_2O$ and $SO_2$ degassing. Because of a lack of partitioning data at <25 MPa, results are unstable below this point, so we truncate models. Model parameters are shown below. The starting composition is the average H14 matrix glass composition (wt%):

| $SiO_2$ | $TiO_2$ | $Al_2O_3$ | $FeO_t$ | MnO | MgO | CaO | $Na_2O$ | $K_2O$ | $P_2O_5$ | $Cr_2O_3$ |
|---------|---------|-----------|---------|-----|-----|-----|---------|--------|----------|-----------|
| *50.27* | *2.08* | *13.23* | *13.49* | *0.24* | *6.47* | *11.01* | *2.59* | *0.24* | *0.19* | *0.02* |

Initial volatile contents, oxidation state and temperatures were estimated from Bali et al. (2018):

| | $H_2O$ | $CO_2$ | S | Redox State | Temperature |
|---|---|---|---|---|---|
| Initial conditions | 0.5 wt% | 1640 ppm | 1700 ppm | QFM+0.5 | 1150°C |

We use two different sets of SulfurX model parameters shown below:

Model 1 parameters

| Model Parameter | Value | Description |
|---|---|---|
| choice | 0 | No crystallization |
| COH_model | 1 | VolatileCalc C-H model (Iacono-Marziono is unstable) |
| fo2_tracker | 1 | fo2 changes during degassing |
| monte_carlo | 1 | Runs MC simulation for error estimate. |
| m_run | 500 | Number of Monte Carlo simulations |
| l | 600 | Total steps of pressure from initial P to 1 bar |
| m | 600 | Total number of runs along degassing |
| S_F_choice | 1 | Uses O'Neill and Mavrogenes (2022) for S speciation |
| sigma | 0.05 | log10fo2 tolerance |
| INC | 50 | Helps for <25 MPa, based on Ding et al. (2023) for Mauna Kea |
| BAR | 5 | |

Model 2

| Model Parameter | Value | Description |
|---|---|---|
| choice | 0 | No crystallization |
| COH_model | 1 | VolatileCalc C-H model (Iacono-Marziono is unstable) |
| fo2_tracker | 1 | fo2 changes during degassing |
| monte_carlo | 1 | Runs MC simulation for error estimate. |
| m_run | 500 | Number of Monte Carlo simulations |
| l | 600 | Total steps of pressure from initial P to 1 bar |
| m | 600 | Total number of runs along degassing |
| S_F_choice | 6.5 | Adapts Muth and Wallace (2021) based on Ding et al. (2023) for Mauna Kea. |
| sigma | 0.05 | log10fo2 tolerance |
| INC | 50 | Helps for <25 MPa, based on Ding et al. (2023) for Mauna Kea |
| BAR | 5 | |

**Supplementary references**

Czamanske, G.K., Moore, J.G., 1977. Composition and phase chemistry of sulfide globules in basalt from the Mid-Atlantic Ridge rift valley near 37°N lat. GSA Bulletin 88, 587–599.

Patten, C., Barnes, S.-J., Mathez, E.A., 2012. Textural variations in MORB sulfide droplets due to differences in crystallization history. The Canadian Mineralogist 50, 675–692. https://doi.org/10.3749/canmin.50.3.675

Rottier, B., Audétat, A., Koděra, P., Lexa, J., 2020. Magmatic evolution of the mineralized Štiavnica volcano (Central Slovakia): Evidence from thermobarometry, melt inclusions, and sulfide inclusions. Journal of Volcanology and Geothermal Research 401, 106967. https://doi.org/10.1016/j.jvolgeores.2020.106967

Rottier, B., Audétat, A., Koděra, P., Lexa, J., 2019. Origin and Evolution of Magmas in the Porphyry Au-mineralized Javorie Volcano (Central Slovakia): Evidence from Thermobarometry, Melt Inclusions and Sulfide Inclusions. Journal of Petrology 60, 2449–2482. https://doi.org/10.1093/petrology/egaa014